BOUNDARY-LAYER TRANSITION MEASUREMENTS ON AN AXISYMMETRIC BODY AT INCIDENCE AT SUPERSONIC SPEED

Hiroki Sugiura
Japan Aerospace Exploration Agency

Abstract

Transition measurements on an axisymmetric nose model at 1- and 2-deg incidence was conducted at Mach 1.2. The configuration of the model is the forward part of a Sears-Haack body. Transition locations were obtained using an infrared camera and characteristics of boundary-layer disturbance was measured using an unsteady pressure transducer. The results show that both stationary and traveling crossflow waves were observed at 1-deg incidence on the side of the model. With the presence of large pressure gradient, crossflow instability amplified linearly while amplitudes of Tollmien-Schlichting instabilities remained constant soon after their initial rapid growths. Comparisons of the measured transition front and N-value distribution calculated using a compressible linear e^N code are also shown.

1 Introduction

Total-aircraft drag reduction of 14 % has been estimated to be realized for supersonic transport by achieving laminar flow up to 60% chordwise station of the wings [1]. To design such wings with natural laminar flow (NLF) effect, it requires transition prediction code that precisely predicts transition location on the aircraft.

An NLF wing was designed using a transition prediction code based on an e^N method at Japan Aerospace Exploration Agency (JAXA), Japan on a nonopowered experimental supersonic transport airplane (NEXST-1). The NLF effect of the wing was confirmed by supersonic wind tunnel tests [2]. However, in order to validate the transition prediction code itself, more universal and basic transition data was required.

Thus, three-dimensional (3D) boundary-layer transition on an axisymmetric nose was examined at supersonic speed. The axisymmetric nose is a simple geometry that realizes axisymmetric two-dimensional boundary layer at zero angle of attack (AOA) and exhibits 3D supersonic boundary layers at AOA. Varying the AOA can easily control three-dimensionality of the boundary layer.

The configuration of the nose is the forward part of a Sears-Haack body defined to have minimum wave drag due to volume at zero AOA. The Sears-Haack body serves as a guideline reference for designing fuselages of supersonic aircraft and has the same geometry as the nose of the NEXST-1. Thus, the present data is directly applicable to the SST nose design.

Similar attempts have been made on sharp cones with zero pressure gradients [3] for supersonic flow and another axisymmetric body for subsonic flow [4]. This is the first attempt to apply to a general axisymmetric body with pressure gradient at supersonic speed.

Crossflow instability occurs in general 3-D boundary layers. This instability produces vortex structures that are aligned approximately to the streamwise directions. However, traveling waves of crossflow instabilities were significantly more unstable than these stationary waves. In most previous compressible crossflow experiments, streamwise pattern due to the streamwise vortices were observed [5-6]. Traveling waves of crossflow instability have never been measured in supersonic boundary layers. For the purpose of investigating

crossflow instability in the supersonic boundary layer, transition on the axisymmetric nose was measured using an infrared camera and an unsteady pressure transducer. The former was used to acquire the distribution of transition fronts and to detect streamwise vortices; the latter was used to acquire the nature of the traveling disturbances.

The previous report [7] focused on the identifications of underlying stability mechanisms determining transition locations. This report concerns the comparison of the calculated and the measured transition fronts and an attempt to compare the calculated and measured characteristics of the disturbances.

2 Experimental Procedures

2.1 Test Facility

The experiment was conducted at Mach 1.2 in the 2 × 2 m transonic wind tunnel of JAXA in Japan.

The static pressure fluctuation normalized by dynamic pressure C_{Prms} at M=1.2 was 0.34% in the tunnel, which was measured with bandwidth from 25 Hz to 20 kHz [8]. The tunnel was the available transonic tunnel with the lowest turbulence level. However, without such care as taken in the quiet tunnels, the tunnel-wall boundary layer is apparently turbulent. Fig. 1b shows the power spectrum of the static pressure fluctuation of a laminar boundary layer on the present model at 0-deg AOA and M=1.2 measured with bandwidth from 125 Hz to 100 kHz. This power spectrum shows that there is no particular frequency dependency in the fluctuation.

Varying the total pressure can control unit Reynolds number. Fig. 1a and 1b show the effect of total pressure on the surface pressure fluctuation and its spectral content, respectively, at 0-deg AOA and M=1.2. It is clear that the total pressure has little effect on the pressure fluctuation and its spectral content so that by varying the total pressure of the tunnel from 50 to 70 kPa, the unit Reynolds number effect on the transition can be studied.

2.2 Test Model

We used an axisymmetric nose model that is 700 mm long measured axially from apex to base (Fig. 2).

Use of resin with high processability allows us to attain the transition front with little influence of surface roughness. Thus, the model is made of an amorphous fiber reinforced plastic called polysulfone. The RMS amplitude of the roughness of the model is 0.22 μm. No bluntness effect exists on the model since its geometry is defined to be blunt.

An unsteady pressure transducer is installed at x=620 mm location on the model and static pressure fluctuation can be measured on the surface. The pressure transducer is 1.6 mm in diameter and is mounted flush with the model surface. No level difference was identified through examination by touch and was confirmed with a thickness gage to be below 50 μm.

For static pressure measurements, we used another model with the same configuration. The model had 6 static ports.

2.3 Measurement of Transition Fronts

IR camera technique is based on measurements detecting variable wall temperatures in the transition region due to different recovery temperatures of laminar and turbulent flows. We used a 12-bit IR camera to map the transition front.

A measurement of optic-angle dependency of the temperature measured using this camera [9] was carried out for a variable-angle flat plate whose temperature is kept constant using a thermostat. The measurement showed that the measured temperatures at 70- and 75-deg optic angle were 95 and 93% of those at 0-deg optic angle, respectively. Thus, every data analysis was made in the range of optic angle below 75 deg.

Fig. 3 shows two typical temperature profiles along the streamlines. The temperature remains constant when the flow is either laminar or turbulent and changes linearly with distance during the transition. Thus, the beginning of the

transition was defined as the location of the intersection point of two approximate lines of least squares respectively through the laminar and turbulent region.

The accuracy of the location of the beginning of transition obtained using the IR camera is estimated to be 1%. The estimation is based on the image length of 1.2 mm corresponding to one pixel and temperature resolution of 0.08K. Temperature resolution of the infrared camera is 0.08 K which is very small compared to our observed differences between surface temperature of laminar and turbulent boundary layer that were in the 3-4 K range.

2.4 Investigation of Disturbances

We also used the unsteady pressure transducer (Kulite XCQ062) to investigate the nature of the disturbance present at the initial stage of transition. The pressure fluctuation was measured with bandwidth from 125 Hz to 100 kHz.

The propriety of the use of unsteady pressure transducer for the disturbance measurement must be considered. From the one-dimensional isentropic relations,

$$p + \rho u^2 = const. \qquad (1)$$

Writing each quantity as the instantaneous deviations of a fluctuating quantity with reference to its temporal mean value gives

$$p = \bar{p} + p', \quad u = \bar{u} + u', \quad \rho u = \overline{\rho u} + (\rho u)'. \quad (2)$$

Eq. (1) is then equivalent to

$$\frac{p'}{\bar{p}} = \gamma M^2 \left(\frac{(\rho u)'}{\overline{\rho u}} + \frac{u'}{\bar{u}} \right). \qquad (3)$$

Hence, pressure fluctuation is proportional to a sum of mass flow fluctuation and velocity fluctuation.

The accuracy of the pressure fluctuation is estimated to be 2%. The estimation is based on the diameter of the transducer, 1.6 mm, resolution of 0.1%, and an assumed estimation error of 1.5% in the process of static pressure calibration.

3 Results and Discussions

3.1 Instability on the Side of the Nose

3.1.1 Distribution of Transition Front

Fig. 4a and 4b show side views of surface temperature distribution of the model at 1- and 2-deg AOA, respectively, determined using the IR camera. The transition front corresponds to the boundary line between light and dark blue regions. Overall, the shapes of the transition front are similar at both AOA. The foremost transition occurred at θ=90 deg at each AOA.

To identify instability mechanisms at θ =90 deg, Fig. 5 gives an enlarged view of surface temperature distribution around x=0.62 m and θ =90 deg at 1-deg AOA. Stationary crossflow vortices are evident in the figure as light-dark patterns. The spacing of the vortices is 12 mm. The calculated wavelength of the crossflow wave is 12.1 mm and is in good agreement with the measured spacing. Similar streamwise patterns were observed in incidenced cone experiments [5-6]. Additionally, the transition occurred more forward than on the windward ray in the presence of the larger pressure gradient which amplifies C-F instabilities but stabilizes T-S instabilities. From these observations, we assume that C-F instability dominates the transition at θ =90 deg.

3.1.2 Boundary-layer Disturbance Spectra

We also carried out additional measurements using the unsteady pressure transducer at θ =90 deg. Fig. 6 shows the power spectrum at x=0.62 m and θ=90 deg at 1-deg AOA. The maximum amplified frequency

calculated using a compressible e^N code with an envelope method strategy [10] is also plotted in the figure. In the calculation, compressible laminar boundary-layer profiles were calculated using a 3-D N-S code with 70 grid points in the boundary layer. The profiles were validated using an axisymmetric laminar boundary-layer code based on the methods developed by Kaups and Cebeci. Nonparallel and curvature effects are not included in the present code. The e^N code is validated experimentally and using another linear stability code developed by Arnal et al. based on the envelope method [10]. The calculated frequency and the measured peak frequency are in good agreement.

Disturbance growth is clearly observed in the 6-15 kHz frequency band, with peak amplitude at 11 kHz. The calculated frequency and the measured peak frequency are in good agreement. The calculated frequency of the T-S wave on the windward and leeward ray are 14 and 8.4 kHz, respectively, as shown in Fig. 7a and 7b; both frequencies are different from this value. Thus, the observed disturbance does not originate in either ray. Several observations in the last few paragraphs imply that the disturbance is C-F traveling wave mode.

3.2 Characteristics of Instability on the Side

Fig. 8 shows effect of total pressure on the pressure fluctuation amplitude at the maximum amplified frequencies at 1-deg AOA. It shows the effect of unit Reynolds number on the fluctuation since the unit Reynolds number is proportional to total pressure. The previous report by the present author concluded that T-S instabilities are dominant on both windward and leeward rays at this AOA; as stated above, crossflow instabilities dominate at θ=90 deg. Crossflow instability amplified linearly while amplitudes of Tollmien-Schlichting (T-S) instabilities remained constant soon after their initial rapid growths. This suggests that with the presence of large pressure gradient, T-S instabilities were amplified gradually and crossflow instabilities were amplified rapidly.

3.3 Comparison with N-value distribution

Fig. 9 shows comparisons of the calculated N-value distribution and the measured transition front. For Z/L<0.05, the measured and calculated distributions have good agreement. Instability mechanisms were different on the windward ray and on the side and it is not guaranteed that the same N value corresponds to the transition front in either areas; however, here N=6 curve agrees well with the transition fronts in either areas. However, comparably large discrepancy exist for Z/L>0.1. Curvature and Nonparallel terms were not included in the calculation. The discrepancy exists where streamline curvatures are the largest. As shown in Ref. 11, curvature stablizes in the compressible boundary layers. Thus, the discrepancy is presumed to be attributed to curvature effect.

4 Summary

Transition the forward part of a Sears-Haack body an axisymmetric nose model at 1- and 2-deg incidence was conducted at Mach 1.2. Both stationary and traveling crossflow waves were observed at 1-deg incidence on the side of the model. With the presence of large pressure gradient, crossflow instability amplified linearly while amplitudes of Tollmien-Schlichting instabilities remained constant soon after their initial rapid growths. The measured transition front and N-value distribution calculated using a compressible linear e^N code were in good agreement. However, discrepancy exists where streamline curvatures have the largest values and it is presumably attributed to curvature effect.

References

[1] Yoshida K, Suzuki K, Iwamiya T and Kuroda H. Reconsideration on aerodynamic design concepts of the scaled supersonic experimental airplane – comparison of the 1st generation SST –. *Proc 31st Japan Society for Aeronautical and Space Science Annual Meeting*, Tokyo, Japan, pp 154-157, 2000 (in Japanese).

[2] Sugiura H, Yoshida K, Tokugawa N, Takagi S and Nishizawa A. Transition measurements on the natural

laminar flow wing at Mach 2. *Journal of Aircraft*, Vol. 39, No. 6, pp 996-1002, 2002.

[3] Malik M and Balakumar P. Instability and transition in three-dimensional supersonic boundary layers. AIAA 92-5049, 1992.

[4] Spall, RE and Malik MR. Linear stability of three-dimensional boundary layers over axisymmetric bodies at incidence. *AIAA Journal*, Vol. 30, No. 4, pp 905-913, 1992.

[5] King RA. Three-dimensional boundary-layer transition on a cone at Mach 3.5. *Experiments in Fluids*, Vol. 13, pp 305-314, 1992.

[6] Oberkampf WL and Aeschliman DP. Joint computational/experimental aerodynamics research on a hypersonic vehicle, part1: experimental results. *AIAA Journal*, Vol. 30, No. 8, pp 2000-2009, 1992.

[7] Sugiura H, Tokugawa N and Ueda Y. Compressible boundary-layer transition on an axisymmetric body at incidence. AIAA 2004-0251, 2004.

[8] Oguni Y, Nakamura S, Hose N and Kawamoto I. The evaluation of flow characteristics of the NAL 2m x 2m transonic wind tunnel. *Proc Supersonic Tunnel Association International Meeting*, Stockholm, Sweden, paper 17, pp 1-43, 2000.

[9] Koyama T and Tsuda S. Measurement of heat transfer distribution by infrared thermography technology. *Journal of the Visualization Society of Japan*, Vol. 19, No. 75, pp 267-272, 1999.

[10] Yoshida K, Ueda Y, Sugiura H, Tokugawa N, Atobe T, Arnal D, Archamboud JP and Seraudie A. Boundary layer transition analysis on NEXST-1 airplane: NAL-ONERA cooperative research project. Proc *3rd International Workshop on Supersonic Civil Aircraft*, National Aerospace Lab, Tokyo, pp 1-, 2001.

[11] Haynes TS and Reed HL. Simulation of swept-wing vortices using nonlinear parabolized stability equations. *Journal of Fluid Mechanics*, vol.405, pp 325-349, 2000.

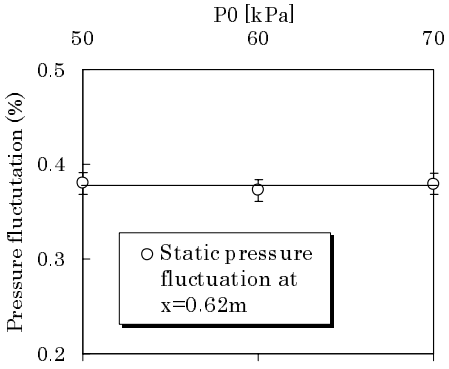

Fig.1a Effect of total pressure on static pressure fluctuation on the model.

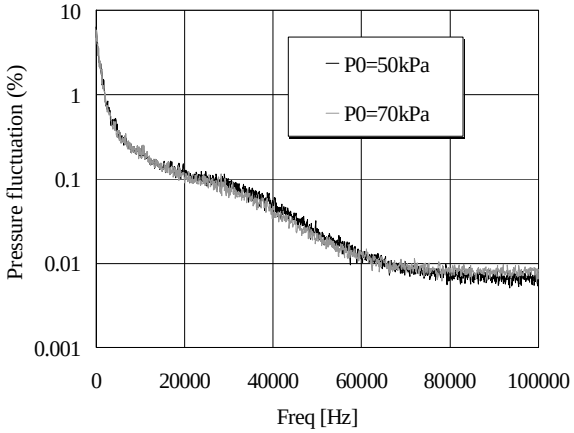

Fig. 1b Effect of total pressure on the power-spectrum of the static pressure fluctuation.

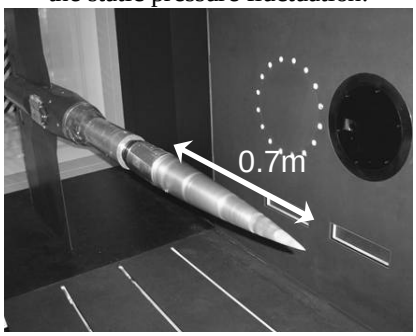

Fig. 2 Axisymmetric nose model.

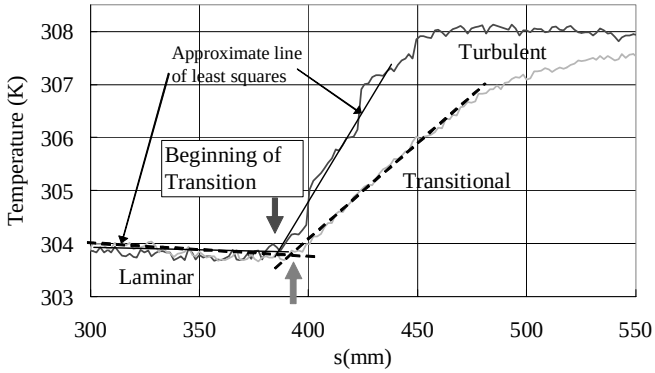

Fig. 3 Examples of temperature profiles measured using IR camera.

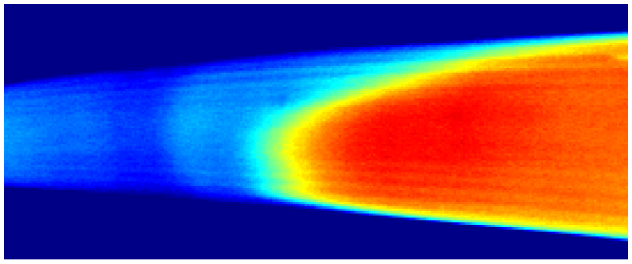

a) At 1-deg AOA.

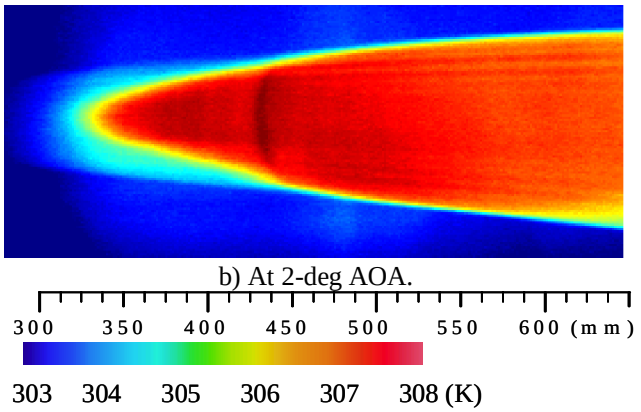

Fig. 4 Side view of surface temperature distribution at 2-deg AOA.

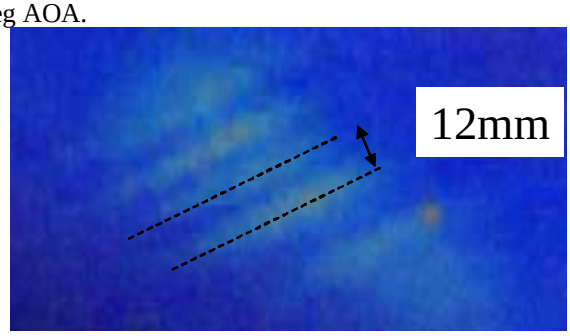

Fig. 5 Enlarged view of surface temperature distribution near x=0.62m and θ=90 deg.

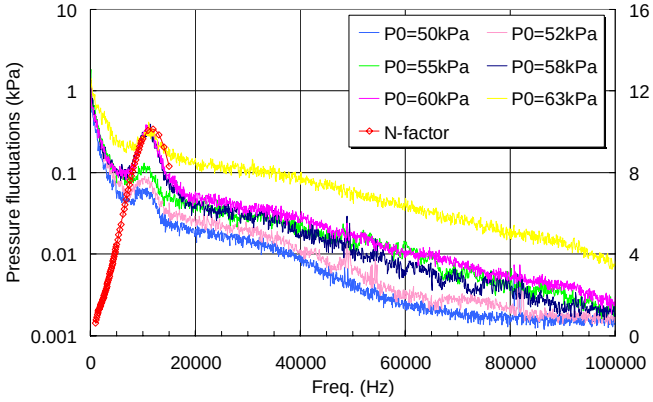

Fig. 6 Power spectrum at x=0.62m and θ=90 deg at 1-deg AOA.

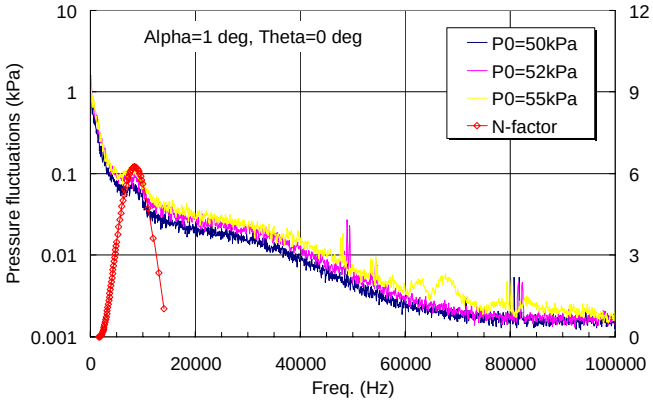

Fig. 7a Power spectrum at x=0.62m on the leeward ray at 1-deg AOA.

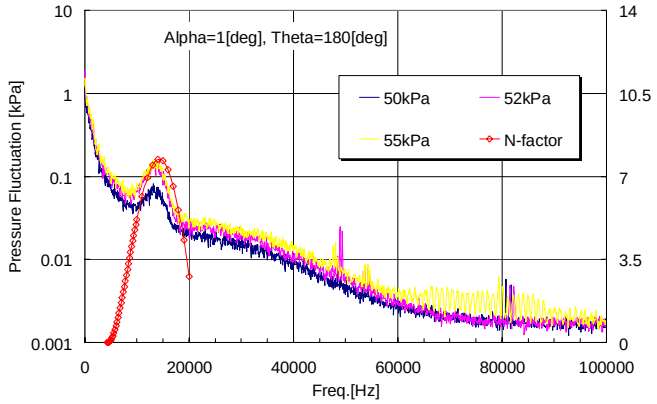

Fig. 7b Power spectrum at x=0.62m on the leeward ray at 1-deg AOA.

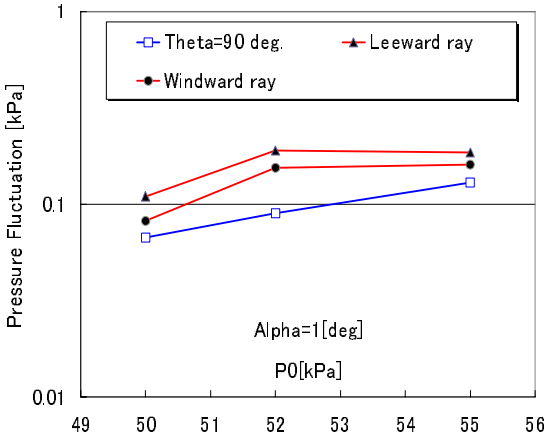

Fig. 8 Effect of total pressure on the pressure fluctuation amplitude at the maximum amplified frequencies.

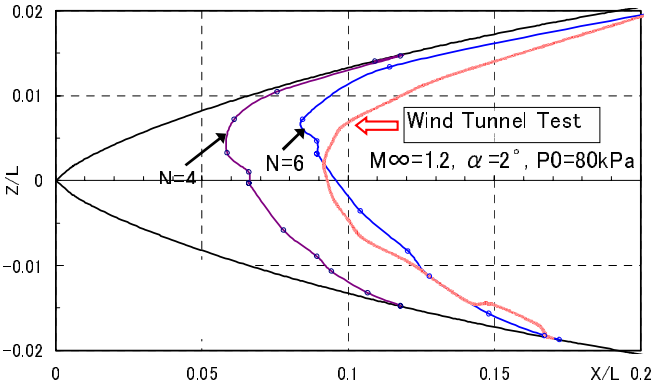

Fig.9 Comparisons of the calculated N-value distribution and the measured transition front.